

# Planar Friction Modelling with LuGre Dynamics and Limit Surfaces

Gabriel Arslan Waltersson and Yiannis Karayiannidis

**Abstract**—Contact surfaces in planar motion exhibit a coupling between tangential and rotational friction forces. This paper proposes planar friction models grounded in the LuGre model and limit surface theory. First, distributed planar extended state models are proposed and the Elasto-Plastic model is extended for multi-dimensional friction. Subsequently, we derive a reduced planar friction model, coupled with a pre-calculated limit surface, that offers reduced computational cost. The limit surface approximation through an ellipsoid is discussed. The properties of the planar friction models are assessed in various simulations, demonstrating that the reduced planar friction model achieves comparable performance to the distributed model while exhibiting  $\sim 80$  times lower computational cost.

## I. INTRODUCTION

Humans possess the remarkable ability to engage in intricate manipulation and interaction with the world around us. We depend on various sensory channels, including vision, touch, and hearing, among others, to perceive our surroundings. Within the realm of robotics, vision has traditionally served as the predominant mode of perception [1]. However, for navigation in human environments or in-hand object manipulation, there exists valuable information that vision alone cannot easily discern, such as object weight, friction properties, applied forces, or grasp state. In such cases, tactile and haptic perception prove more suitable [2]. The interaction between a robot and its environment hinges upon the principles of friction and contact dynamics, e.g. an object gripped by a parallel gripper, or a walking robot's foot making contact with the ground. Surprisingly, a noticeable disparity exists between the capabilities of one-dimensional and planar friction models. Therefore, this paper focuses on modelling friction for arbitrary contact surfaces in planar motion, an example is depicted in Fig. 1. This paper addresses several challenges encountered in dynamic planar friction models, including computational cost, numerical stability, and drifting under oscillating loads.

The study of friction encompasses various disciplines [3], each of which tends to possess its own set of friction models tailored to its specific requirements. Planar friction exists in many fields. In robotics, it is found in the context of in-hand manipulation, walking/ground contact, pushing, etc. In the domain of vehicles, planar friction becomes relevant in areas such as tire modelling and safety systems e.g. traction control or ABS. In recent times, with the emergence of digital twins

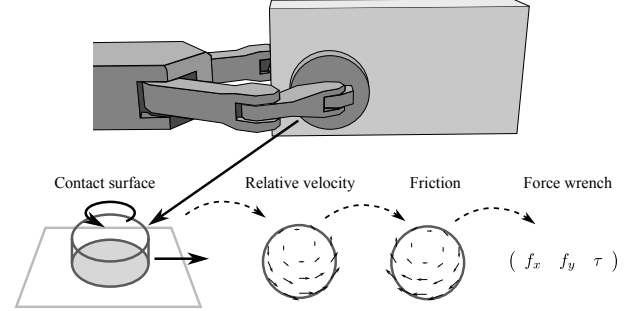


Fig. 1: Planar friction in a parallel gripper, wherein the friction force is represented by a force wrench vector.

and more sophisticated physics simulators like Isaac Gym [4] or Algoryx [5], the relevance of these models has increased. This highlights the importance of planar friction modelling.<sup>1</sup>

## II. RELATED WORK

The classical Coulomb friction model describes friction as a force that opposes the motion and is proportional to the normal force, or a force that in static scenarios balance the applied forces acting on the body. Dahl introduced a friction model in 1968 [6], which estimates friction forces based solely on velocity and micro displacements by incorporating an additional state variable. The model conceptualizes the friction force as a result of numerous tiny bristles present at the contact surface. The extended state variable models the average deflection of the bristles, illustrated in Fig. 2. However, Dahl's model does not account for the Stribeck effect [7], encoding the dependency of the friction coefficient and viscosity on velocity [8]. To address this limitation, Åström and Canudas-de-wit developed the LuGre model, which extends the Dahl friction model to incorporate the Stribeck effect [7].

Over time, the LuGre model has undergone numerous extensions and modifications to enhance its capabilities. One of the early modifications was the inclusion of varying normal force, resulting in the amended LuGre model [9]. The original LuGre model exhibited drifting behaviour for varying tangential loads, even when the load remained below the maximum static friction threshold. To tackle this issue, Dupont et al. proposed the Elasto-Plastic model [10] as an extension of the LuGre model. In the Elasto-Plastic model, the internal state variable representing bristle deflection behaves as a pure spring for deflections smaller than the break-away deflection. In experimental comparisons between Coulomb, Stribeck, Dahl, LuGre and Elasto-Plastic friction models for micro stick-slip motions, Liu et al. found that the LuGre model exhibited the highest level of accuracy [11]. Marques et al. conducted investigations into the

This work was funded by the Wallenberg AI, Autonomous Systems and Software Program (WASP) funded by the Knut and Alice Wallenberg Foundation.

Gabriel Arslan Waltersson is with the Department of Electrical Engineering, Chalmers University of Technology, SE-412 96 Gothenburg, Sweden gabwal@chalmers.se. *Corresponding author.*

Yiannis Karayiannidis is with the Department of Automatic Control, Lund University, Sweden yiannis@control.lth.se. The author is a member of the ELLIIT Strategic Research Area at Lund University.

<sup>1</sup>The code developed for this paper is available with open access at <https://github.com/Gabrieleenx/FrictionModelling>.

LuGre model under varying normal loads [12]. They observed that during stiction, the amended LuGre model experienced drifting in displacement and oscillations in tangential force. These issues were attributed to the varying bristle deflection required to maintain a constant tangential force. To mitigate the oscillations, the proposed solution involved introducing a variable bristle stiffness coefficient that remained fixed during sticking. However, this approach resulted in a trade-off, as the model's stiffness was no longer consistent and depended on how the sticking state was established. In Section VI-C, we present results demonstrating that the Elasto-Plastic model can alleviate drifting in displacements for varying normal loads. The LuGre model can introduce challenges in simulating dynamical systems due to its numerical stiffness, recognizing this issue, Do *et al.* [13] studied different methods for simulating systems with the LuGre model. To enhance computational efficiency in simulating multi-zone contacts of thin beams, Wang utilized a piecewise analytical LuGre model [14].

The friction models discussed thus far have been one-dimensional. However, when dealing with planar motion, friction becomes multi-dimensional. In the context of planar sliders, the limit surface theory, introduced by Goyal *et al.* [15] [16], is the prominent theory that describes the coupling between tangential friction and torque for different motions, assuming Coulomb friction. The limit surface theory has gained interest in the robotics community and in modelling contact mechanics for grasping tasks. The limit surface is often approximated using an ellipsoid, due to its similar shape and simplified representation [17], [18], [19], [20], [21], [22]. It is worth noting that the comparison between the limit surface and the ellipsoid approximation is commonly depicted using plots that focus solely on the closest distance. However, in Section V-B, we present evidence to demonstrate that the ellipsoid approximation of the limit surface is less accurate when considering the corresponding location on the limit surface than what is frequently portrayed in the literature.

Hertz pioneered the study of contact mechanics [23]. He established that the radius of the contact area between a sphere and a flat surface is proportional to the normal force raised to the power of 1/3. Building upon Hertz's work, Xydias and Kao extended the model and conducted experiments that revealed the radius to be proportional to the normal force raised to the power between 0 and 1/3, depending on the material properties [19]. In the context of the onset of sliding, Dahmen *et al.* investigated the coupling between static friction and torque, finding that Coulomb friction alone is insufficient to determine this behaviour [24]. Their experiments also indicated that the limit surface is similar across different materials. Shi *et al.* utilized the ellipse approximation in their work on dynamic in-hand sliding manipulation of flat objects [22]. Alternatively, Hu *et al.* approached the modelling of general planar contacts by incorporating a random field to represent the friction coefficient [25].

Only a few papers have attempted to extend dynamic friction models to planar motions. Velenis, Tsiotras, and Canudas-de-Wit presented an early extension of the LuGre model to 2D for tire friction [26]. Kato [27], [28] worked on anisotropic adhesion models with the Dahl model and extended it for 2D

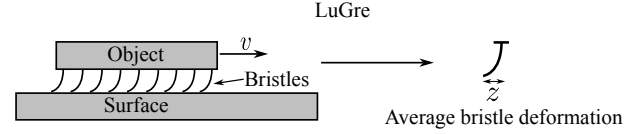


Fig. 2: The bristle analogy of the Dahl and LuGre friction model.

motion, by dividing the contact path into small regions both friction and torque could be calculated. Zhou *et al.* modelled 2D friction using the LuGre model for point contacts [29]. Costanzo *et al.* combined the LuGre model with the limit surface to estimate instantaneous rotation around the centre of rotation (CoR) for in-hand pivoting manipulations [30]. Colantonio *et al.* projected the LuGre model into 3D, capturing friction in multiple directions, but not torsion directly [31]. An attempt to extend the Elasto-Plastic model for planar motion was done in [32]. In our work, we take a different approach, focusing on the general simulation of planar motions, considering different contact pressures, and leveraging the principles of the limit surface theory.

The paper proposes a computationally efficient model to simulate dynamic and static friction for contact surfaces in planar motion, e.g. grasping or pushing operations. The concrete contributions are:

- A distributed planar friction model for an arbitrary contact surface and pressure distribution, combining the LuGre model and the limit surface theory, in contrast to [9], [28] which considered specific contact scenarios and cannot model grasping.
- A reduced planar friction model with a pre-computed limit surface, that in comparison to the distributed planar friction model is computationally efficient.
- Extension of the elasto-plastic model, originally defined for 1D systems [10], to planar friction, and enhancement of numerical stability of LuGre type models.

The paper is structured as follows: In section III, the background theory for the LuGre, Elasto-Plastic and limit surface is given. In section IV, the distributed planar friction model is presented along with the multi-dimensional Elasto-Plastic model and the bristle bound. In section V, a computationally fast planar friction model is derived. In section VI the tests and results for the friction models are presented.

### III. BACKGROUND

#### A. Notation

We introduce the following notation:

- Bold lower case letters denote vectors and bold upper letters denote matrices.
- $|\cdot|$  denote absolute value of a scalar and element-wise absolute value of vectors and matrices.
- $\|\cdot\|$  denote the Euclidean norm of a vector and  $\|\cdot\|_{\mathbf{M}}$  a weighted Euclidean norm where  $\mathbf{M}$  is a positive definite matrix.
- $\text{diag}(\mathbf{a})$  with  $\mathbf{a}$  being an  $n$ -dimensional vector denotes a square diagonal matrix of dimension  $n$  with diagonal entries being equal to the elements of  $\mathbf{a}$ .
- The cross product  $\mathbf{a} \times \mathbf{b}$  of two dimensional vectors  $\mathbf{a} = [a_x \ a_y]^T$ ,  $\mathbf{b} = [b_x \ b_y]^T$  is given by  $\mathbf{a} \times \mathbf{b} = a_x b_y - a_y b_x$ .

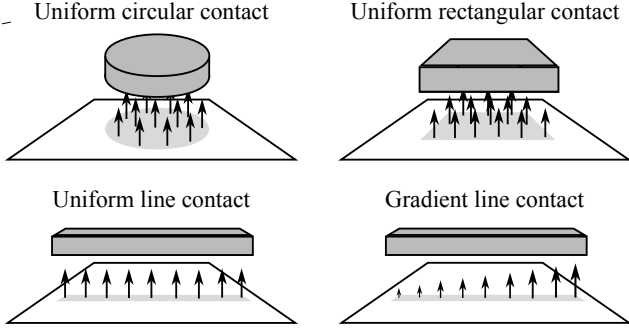


Fig. 3: Four examples of different contact surfaces.

### B. LuGre

In its original form, the LuGre model assumes constant normal force ( $f_n$ ). However, De Wit and Tsotras (1999) expanded upon this model to accommodate varying normal loads by introducing the active friction coefficient. The active friction coefficient is multiplied by the normal load to determine the resulting friction forces. This adaptation, known as the amended LuGre model, governs the deflection of the bristles, denoted as  $z$ , as follows:

$$\dot{z} = v - z \frac{\sigma_0 |v|}{g(v)} \quad (1)$$

where  $v$  is the relative velocity between the surfaces, and  $\sigma_0$  is the amended bristle stiffness. The amended steady-state friction coefficient  $g(v)$  is given by:

$$g(v) = \mu_C + (\mu_S - \mu_C) e^{-|\frac{v}{v_s}|^\gamma} \quad (2)$$

where  $\mu_C$  represents the Coulomb friction and  $\mu_S$  the static friction coefficient. The parameter  $v_s$  and  $\gamma$  govern how fast  $g(v)$  converges to  $\mu_C$  with increasing velocity. The friction force is expressed as:

$$f = (\sigma_0 z + \sigma_1 \dot{z} + f_v(v)) f_n \quad (3)$$

where  $\sigma_1$  corresponds to the dampening coefficient and  $f_v(v)$  the velocity dependent memoryless friction. Typically,  $f_v(v) = \sigma_2 v$  denotes the linear viscous friction.

### C. Elasto-plastic model

It has been observed that the LuGre model exhibits a tendency to drift when subjected to oscillating tangential loads, even when these loads remain significantly below the threshold required for slippage [10], see Fig. 6. To address this issue, the Elasto-Plastic model introduces a purely elastic behaviour for bristle deflections below a specified breakaway threshold, denoted as  $z_{ba}$ . The bristle rate deflection (1), is modified to:

$$\dot{z} = v - \alpha(z, v) z \frac{\sigma_0 |v|}{g(v)} \quad (4)$$

where  $\alpha(z, v)$  is a function described by:

$$\alpha(z, v) = \begin{cases} 0 & \text{sgn}(v) \neq \text{sgn}(z) \\ \begin{cases} 0 & |z| \leq z_{ba} \\ \alpha & z_{ba} \leq |z| \leq z_{max} \\ 1 & |z| \geq z_{max} \end{cases} & \text{sgn}(v) = \text{sgn}(z) \end{cases} \quad (5)$$

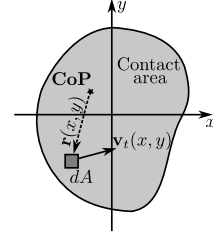


Fig. 4: The vector  $\mathbf{r}(x, y)$  from CoP to the infinitesimal contact area  $dA$  and the local velocity vector  $\mathbf{v}_t(x, y)$ , for a contact surface.

where:

$$\alpha = \frac{1}{2} \sin \left( \pi \frac{z - (z_{max} + z_{ba})/2}{z_{max} - z_{ba}} \right) + \frac{1}{2} \quad (6)$$

This sinusoidal function facilitates a smooth transition from elastic to plastic deformation. The elastic behaviour within the sticking regime ensures that the friction force remains proportional to the micro-displacement, thereby preventing drifting. The maximum bristle deflection is determined by the steady-state deflection and can be expressed as  $z_{max} = z_{ss} = \frac{g(v)}{\sigma_0}$ .

### D. Limit surface

A contact surface under planar motion, involving sliding and spinning, has a coupling between tangential friction and angular friction. For example, an object that is spinning requires less force to push it tangentially compared to when the object has no angular velocity. The description of this coupling phenomenon is provided by the limit surface theory [16], assuming Coulomb friction. The tangential forces  $\mathbf{f}_{LS} \in \mathbb{R}^2$  and the torque  $\tau_{LS}$  defining the limit surface are given by:

$$\mathbf{f}_{LS} = - \int_A \mu_C \hat{\mathbf{v}}_t(x, y) p(x, y) dA \quad (7)$$

and

$$\tau_{LS} = - \int_A \mu_C [\mathbf{r} \times \hat{\mathbf{v}}_t] p(x, y) dA \quad (8)$$

where  $\mathbf{r} = [x \ y]^T$  is a position vector with its origin at the centre of pressure (CoP), as depicted in Fig. 4, while  $\hat{\mathbf{v}}_t(x, y)$  denotes the unit velocity vector at coordinates  $(x, y)$ . The function  $p(x, y)$  represents the pressure at  $(x, y)$  and can be used to describe an arbitrary contact surface, see examples in Fig. 3. For axisymmetric pressure distributions that exhibit circular contact pressure, the limit surface curve can be reduced to a two-dimensional curve within one quadrant. However, for more general pressure distributions, the limit surface takes the form of a three-dimensional surface.

## IV. PLANAR FRICTION MODELING

In this section, we introduce a distributed planar friction model that combines the principles of the LuGre model and the limit surface theory. The Elasto-Plastic model is extended for the planar case to mitigate the drifting exhibited by the distributed LuGre model under oscillating loads. We propose a bristle deflection bound to increase numerical stability and show how to numerically compute the integrals in the distributed model.

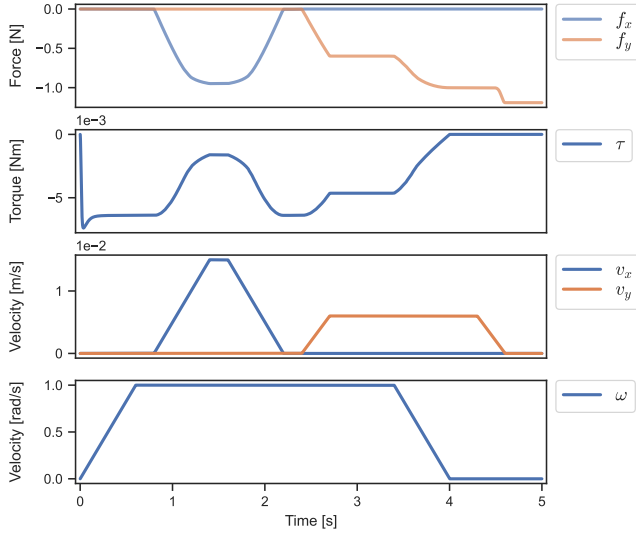


Fig. 5: Simulation with predefined velocity profile for the distributed planar LuGre model. The simulation uses a circular contact surface with a radius of 10 [mm] and a normal force of 1 [N]. The velocity profile and friction force are at the CoP.

#### A. Distributed LuGre model

The proposed model combines the LuGre model with the limit surface theory by extending the LuGre model to model 2D bristles and integrating it over the contact surface. A similar derivation in the context of tire friction has been done in [26], where the LuGre model was extended to 2D and integrated over one dimension. The integration over the contact surface allows for the representation of arbitrary contact pressures using the spatially varying function  $p(x, y)$ . We define the function  $L(\cdot)$  to describe the 2D LuGre friction, where the forces at  $(x, y)$  are given by:

$$L(\mathbf{v}_t(x, y), \mathbf{z}_t(x, y), p(x, y)) = (\sigma_0 \mathbf{z}_t(x, y) + \sigma_1 \dot{\mathbf{z}}_t(x, y) + \sigma_2 \mathbf{v}_t(x, y)) p(x, y) \quad (9)$$

where  $\mathbf{v}_t = [v_x \ v_y]^T$  represents the relative velocity between the surfaces (as shown in Fig. 4), and  $\mathbf{z}_t = [z_x \ z_y]^T$  denotes the tangential bristle deflection. The rate of bristle deflection  $\dot{\mathbf{z}}_t(x, y)$  is given by:

$$\dot{\mathbf{z}}_t(x, y) = \mathbf{v}_t(x, y) - \mathbf{z}_t(x, y) \frac{\sigma_0 \|\mathbf{v}_t(x, y)\|}{g(\|\mathbf{v}_t(x, y)\|)} \quad (10)$$

where  $g(\cdot)$  is defined as in (2). The major difference in the 2D bristle deflection rate compared to equation (1) is the coupling between the  $x$  and  $y$  components due to the norm of the velocity  $\|\mathbf{v}_t(x, y)\|$ . This coupling ensures that the norm of the steady-state deflection is independent of the velocity direction. The steady-state deflection  $\mathbf{z}_{tss}$  is given by:

$$\mathbf{z}_{tss}(x, y) = \frac{\mathbf{v}_t(x, y) g(\|\mathbf{v}_t(x, y)\|)}{\sigma_0 \|\mathbf{v}_t(x, y)\|} \quad (11)$$

and the local steady-state friction is represented as:

$$L_{ss}(\mathbf{v}_t(x, y), \mathbf{z}_{tss}(x, y), p(x, y)) = (\sigma_0 \mathbf{z}_{tss}(x, y) + \sigma_2 \mathbf{v}_t(x, y)) p(x, y) \quad (12)$$

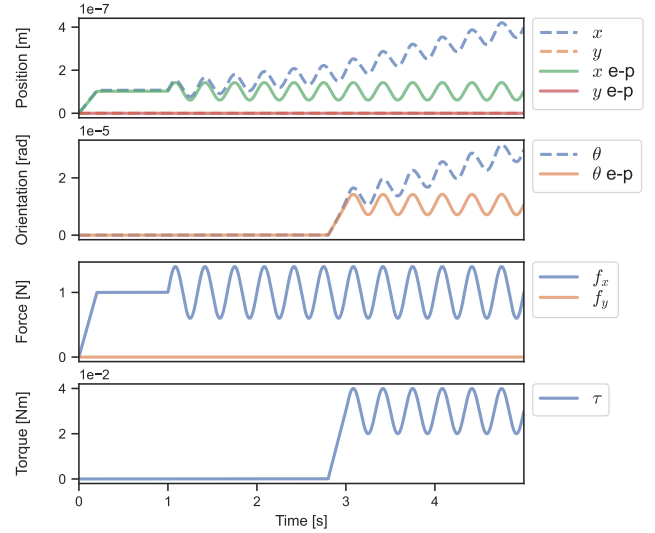


Fig. 6: Planar LuGre drifting under oscillating tangential loads compared with the Elasto-Plastic (e-p) extension. The loads are under the threshold for initiating or sustaining slippage. Simulated with a 1 [kg] disc with a radius of 0.05 [m] and the settings specified in table III.

To calculate the total tangential friction force, equation (9) is integrated over the contact surface:

$$\begin{bmatrix} f_x \\ f_y \end{bmatrix} = - \int_A L(\mathbf{v}_t(x, y), \mathbf{z}_t(x, y), p(x, y)) dA \quad (13)$$

where  $f_x$  and  $f_y$  represent the tangential force at CoP. The frictional torque at CoP can be calculated using:

$$\tau = - \int_A \mathbf{r}(x, y) \times L(\mathbf{v}_t(x, y), \mathbf{z}_t(x, y), p(x, y)) dA \quad (14)$$

For the calculation of steady-state friction, equation (12) is used instead of equation (9) in equations (13) and (14).

Throughout the paper, a running example is used to illustrate each section's contribution. An object with a circular contact area, 10 [mm] radius, is placed on a flat surface and manifests 1 [N] normal force. The object follows a preset velocity profile, and the resulting friction forces are simulated as shown in Fig. 5. The velocity profile is designed such that the CoR moves inside or near the contact area to emphasize the coupling between the tangential and angular friction forces. If not explicitly stated otherwise, the examples and simulations use the settings provided in table III.

#### B. Multi-dimensional Elasto-Plastic model

This section introduces an extension of the Elasto-Plastic model, for multi-dimensional bristles, to address the drifting problem observed in the LuGre model for oscillating tangential loads, see Fig. 6. The 1D Elasto-Plastic model has separate cases depending on if  $z$  and  $v$  have the same direction or not (5). In this work, we generalize this concept to the planar case

TABLE I: Friction parameters

p	$\sigma_0$	$\sigma_1$	$\sigma_2$	$\mu_c$	$\mu_s$	$\gamma$	$v_s$	$s_{ba}$
0	1e6	8e1	0	1	1	2	1e-3	0.9
1	1e6	8e1	0.2	1	1.2	2	1e-3	0.9

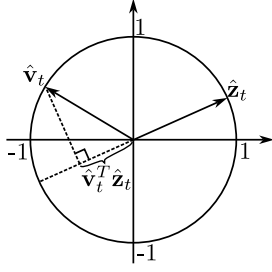


Fig. 7: Projection of the unit velocity  $\hat{\mathbf{v}}$  on the unit bristle deflection  $\hat{\mathbf{z}}$ .

by a projection. The Elasto-Plastic bristle deflection rate for the planar case is given by:

$$\dot{\mathbf{z}}_t(x, y) = \mathbf{v}_t(x, y) - \mathbf{z}_t(x, y)\beta(\mathbf{z}_t, \mathbf{v}_t) \frac{\sigma_0 \|\mathbf{v}_t(x, y)\|}{g(\|\mathbf{v}_t(x, y)\|)} \quad (15)$$

where  $\beta(\mathbf{z}_t, \mathbf{v}_t)$  is the extended version of  $\alpha(z, v)$  in (5). The key idea is to consider the alignment between the unit velocity vector  $\hat{\mathbf{v}}_t$  and the unit bristle deflection vector  $\hat{\mathbf{z}}_t$  to determine the elastic behaviour. The projection of  $\hat{\mathbf{v}}_t$  on  $\hat{\mathbf{z}}_t$ , see Fig. 7, is used to calculate a ratio  $\epsilon(\hat{\mathbf{z}}_t, \hat{\mathbf{v}}_t)$  that represents the alignment:

$$\epsilon(\hat{\mathbf{z}}_t, \hat{\mathbf{v}}_t) = (\hat{\mathbf{v}}_t^T \hat{\mathbf{z}}_t + 1)/2 \quad (16)$$

and the Elasto-Plastic variable  $\beta(\mathbf{z}_t, \mathbf{v}_t)$  is calculated with:

$$\beta(\mathbf{z}_t, \mathbf{v}_t) = \epsilon(\hat{\mathbf{z}}_t, \hat{\mathbf{v}}_t) \bar{\beta}(\mathbf{z}_t) \quad (17)$$

where the function  $\bar{\beta}(\mathbf{z}_t)$  is similar to  $\alpha(z, v)$  in (5) for the case when  $\text{sgn}(z) = \text{sgn}(v)$ , but extended to use the norm instead.  $\bar{\beta}(\mathbf{z}_t)$  is given by:

$$\bar{\beta}(\mathbf{z}_t) = \begin{cases} 0 & \|\mathbf{z}_t\| \leq z_{ba} \\ \alpha(\|\mathbf{z}_t\|) & z_{ba} \leq \|\mathbf{z}_t\| \leq z_{max} \\ 1 & \|\mathbf{z}_t\| \geq z_{max} \end{cases} \quad (18)$$

where  $\alpha(\|\mathbf{z}_t\|)$  is the same as (6). The breakaway bristle deflection is defined as  $z_{ba} = s_{ba} z_{max}$ , where  $s_{ba}$  is a scalar multiplier, and  $z_{max} = \|\mathbf{z}_{tss}\|$ . For the 1D motion, this method is equivalent to the standard Elasto-Plastic method described in III-C.

To validate the effectiveness of the Elasto-Plastic extension, simulations are conducted on a 1 [kg] disc with a 0.05 [m] radius on a flat surface subjected to varying external loads. The loads are below the threshold for slip initiation or sustainment, see section VI-C for more details. The results in Fig. 6 demonstrate that the planar LuGre model without the Elasto-Plastic extension exhibits slight drift, while the model with the extension shows no drift, even when subjected to combined oscillating loads in the tangential and angular directions.

### C. Bristle deflection bound

The LuGre model is numerically stiff [29], which can lead to simulation instabilities. Without any bounds on the bristle deflection, simulating the example shown in Fig. 5 would result in unstable behaviour, e.g. after 1.2 [s] the forces are oscillating with an amplitude of  $5e29$  [N]. This instability arises because the displacement of the bristles is very small compared to the possible velocities, necessitating very small time steps for accurate simulation. To address the issue, we

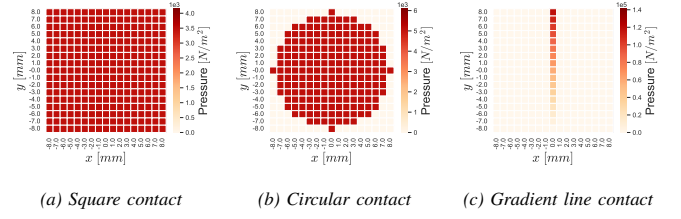


Fig. 8: Three examples of how different contact pressures are discretized. The contact area in the figure is discretized into  $17 \times 17$  cells.

propose constraining the bristle deflection rate to prevent overshooting of the steady-state deflection within a single time step  $\Delta t$ . For an infinitesimal time step the bristle deflection always tend toward the steady-state deflection. The maximum allowed deflection rate is calculated as:

$$\delta \mathbf{z}_t = (\mathbf{z}_{tss} - \mathbf{z}_t) / \Delta t \quad (19)$$

which is used to element-wise limit the deflection rate:

$$\dot{\mathbf{z}}_{ti} = \min(|\dot{\mathbf{z}}_{ti}|, |\delta \mathbf{z}_{ti}|) \text{sgn}(\dot{\mathbf{z}}_{ti}) \quad (20)$$

where  $i \in \{x, y\}$  and  $\dot{\mathbf{z}}_t = [\dot{z}_{tx} \ \dot{z}_{ty}]^T$  is the new deflection rate that restricts  $\dot{\mathbf{z}}_t$  in case of overshooting. By applying this constraint, larger time steps can be used without encountering these stability issues from the friction model.

### D. Numerical approximation

To solve the distributed model from equation (13) and (14), the contact area is discretized into a grid of  $N \times N$  cells, as shown in Fig. 8. Each cells contains a 2D LuGre model, and the integrals in equations (13) and (14) can be discretized as follows:

$$\begin{bmatrix} f_x \\ f_y \end{bmatrix} = - \sum_{i_x=1}^N \sum_{i_y=1}^N L(\mathbf{v}_t(\cdot), \mathbf{z}_t(\cdot), p(\cdot)A) \quad (21)$$

$$\tau = - \sum_{i_x=1}^N \sum_{i_y=1}^N \mathbf{r}(\cdot) \times L(\mathbf{v}_t(\cdot), \mathbf{z}_t(\cdot), p(\cdot)A) \quad (22)$$

where  $A$  is the area of a cell.

The number of cells impacts the computational cost. Therefore, the question arises: how many cells are required? Fig. 9 illustrates the root mean square error (RMSE) normalized with the maximum force for different combinations of contact pressure distributions and friction parameters, as shown in table I. The RMSE is calculated using a fixed velocity profile, as depicted in Fig. 5. The ground truth is obtained using a  $101 \times 101$  cell grid. The average computational cost associated with different numbers of cells is summarized in table II.

### E. Bilinear steady-state approximation

The numerical approximation employed in equations (21) and (22) exhibits undesirable traits due to the discretization.

TABLE II: Computational cost (distributed model)

$N$	5	9	13	17	21	25	29	33	101
$it/s$	1.6e5	3.9e4	2.8e4	1.7e4	1.1e4	7.7e3	5.7e3	4.5e3	4.3e2

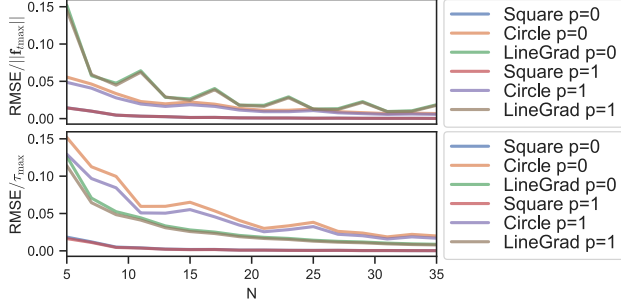


Fig. 9: RMSE normalized with the maximum force over different numbers of cells  $N \times N$ . The results are for the planar distributed model, tested with different contact surfaces (see Fig. 8) and different friction parameters (see table I). The top plot is for tangential friction and the bottom is for the torque. The velocity and force are evaluated at CoP.

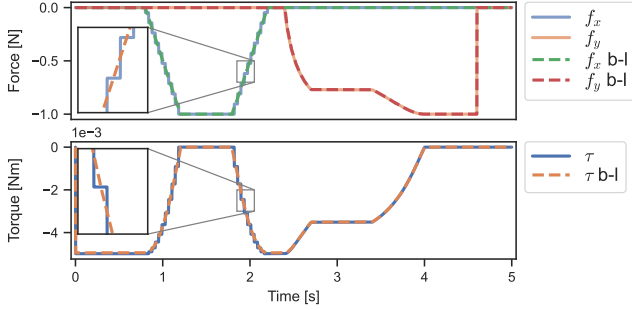


Fig. 10: Discrete step behaviour of the steady-state friction due to the numerical approximation (21) and (22). The results are simulated using a line contact following the velocity profile in 5. The bilinear approximation (b-l) mitigates the step-like behaviour. Simulated with  $p = 0$  from table I.

In situations where the CoR moves within the contact area, discernible discontinuities manifest in the forces, as depicted in Fig. 10. The steady-state friction, essential for pre-computing the limit surface in the subsequent section V, is adversely affected by these discontinuities. For a line contact, with the CoR traversing along its length, the tangential friction force exhibits increments upon surpassing the midpoint of a cell, as illustrated in Fig. 11. To circumvent this issue, a bilinear interpolation [33] method is employed. First, the cell encompassing the CoR is identified, and temporary CoRs (CoR\*) are utilized at each corner of said cell to compute the friction forces. Subsequently, these friction forces are combined via bilinear interpolation, estimating the steady-state friction at the CoR, as illustrated on the right-hand side of Fig. 11. A comparison between utilizing a single point and bilinear interpolation is shown in Fig. 10.

## V. REDUCED PLANAR FRICTION

The primary concern with the distributed planar friction model lies in its computational complexity. As indicated in table II, the computational cost grows with the increasing number of cells employed to approximate the contact surface. In this section, we propose a novel approximation to the distributed planar LuGre model based on three bristles, see Fig. 12. The three bristles are coupled with an ellipsoid approximation of the limit surface. The limitations of the ellipsoid approximation are discussed and we propose a scaling matrix based on a pre-computed limit surface to correct for

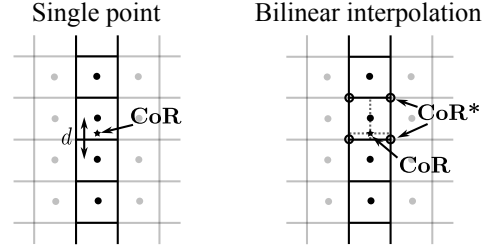


Fig. 11: Illustrates the cells for a line contact. On the left-hand side, the friction is calculated at the middle of each cell and is evaluated at the CoR, and on the right-hand side it is evaluated at the corners of the cell containing the CoR, the forces at CoR are then estimated with bilinear interpolation. The left-hand figure illustrates the distance  $d$  that the CoR can travel before passing the midpoint of a cell.

the discrepancies. Finally, the pre-computation of the ellipsoid variables and the limit surface are discussed.

### A. Ellipsoid approximation

The distributed planar LuGre model is reduced to three bristles by approximating the contact surface as a circular rim contact, see figure 12b. To achieve this, the coupling between the steady-state deflection of the three bristles is governed by an ellipsoid approximation of the limit surface. The ellipsoid approximation with Coulomb friction has been employed in previous works [22], [19], and [21]. The force wrench  $\mathbf{f}_e$  is expressed as a function of the combined relative velocity vector  $\mathbf{v} = [v_x \ v_y \ \omega]^T$ , which contains both the linear and angular velocity of a frame located at CoP. In this paper, the mapping of  $\mathbf{v}$  to the force wrench  $\mathbf{f}_e$  under Coulomb friction is defined based on an upper-triangular matrix  $\mathbf{A}$  as follows:

$$\mathbf{f}_e = \mu_C f_n \frac{\mathbf{A} \mathbf{v}}{v_n} \quad (23)$$

$$\text{where } \mathbf{A} = \begin{bmatrix} 1 & 0 & s_x \\ 0 & 1 & s_y \\ 0 & 0 & r_a^2 \end{bmatrix}, v_n = \|\mathbf{v}\|_{\mathbf{A}_{\text{sym}}}, \mathbf{A}_{\text{sym}} = \frac{\mathbf{A} + \mathbf{A}^T}{2},$$

and  $r_a$  represents the radius of a corresponding circular rim contact, illustrated in Fig. 12b. The skew variables  $s_x$  and  $s_y$  encode the contribution of the rotational to linear velocity for the simplified contact surface. This allows the model to express tangential forces under pure rotation at CoP, which will be further discussed in section V-E.

Having defined the force wrench in (23), few remarks are in order:

- The upper-triangular matrix  $\mathbf{A}$  determines the shape of the ellipsoid  $\mathbf{f}_e^T \frac{1}{(\mu_C f_n)^2} \mathbf{A}^{-1} \mathbf{f}_e = 1$ .
- The symmetric part of  $\mathbf{A}$ , namely  $\mathbf{A}_{\text{sym}}$ , is positive definite matrix as proved in appendix A.
- The radius  $r_a$  can be pre-calculated for a surface as:

$$r_a = \left| \int_A [\mathbf{r}(x, y) \times \tilde{\mathbf{v}}_t(x, y)] p_n(x, y) dA \right| \quad (24)$$

where  $p_n(x, y) = p(x, y)/f_n$  is the normalized pressure and the tangential velocity vector  $\tilde{\mathbf{v}}_t(x, y)$  describes a pure rotation around CoP with the angular velocity  $\omega$ .

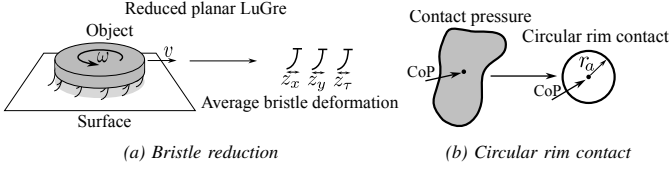


Fig. 12: The planar friction model reduced into a circular rim contact, which can be described by three bristles.

The coupling between the steady-state deflection of the three bristles is modelled by replacing the Coulomb friction in (23) with the 1D steady-state deflection, resulting in:

$$\mathbf{z}_{ss} = \frac{g(v_n)\mathbf{A}\mathbf{v}}{\sigma_0 v_n} \quad (25)$$

By unravelling the expression, the bristle deflection rate can be determined as:

$$\dot{\mathbf{z}} = \mathbf{A}\mathbf{v} - \mathbf{z} \frac{\sigma_0 v_n}{g(v_n)} \quad (26)$$

where  $\mathbf{z} = [z_x \ z_y \ z_\tau]^T$ . The forces at COP are calculated by:

$$\mathbf{f} = -(\sigma_0 \mathbf{z} + \sigma_1 \dot{\mathbf{z}} + \sigma_2 \mathbf{U} \mathbf{A} \mathbf{v}) f_n \quad (27)$$

where  $\mathbf{U} = \text{diag}([1 \ 1 \ u])$  is a scaling matrix used to correct the viscous friction when reducing the contact surface into a circular rim contact. The scaling  $u$ , can be pre-calculated for a surface, as follows:

$$u = \frac{-\int_A \mathbf{r}(x, y) \times \begin{bmatrix} y \\ -x \end{bmatrix} p_n(x, y) dA}{r_a^2} \quad (28)$$

The value of  $u$  given in (28) corresponds to  $\tau_{vr} = \tau_{vs}$ , where from (27), the rotational viscous friction for the circular rim contact  $\tau_{vr}$  is given by:

$$\tau_{vr} = u \sigma_2 r_a^2 \omega f_n \quad (29)$$

and from (14) the rotational viscous friction for the contact surface:

$$\tau_{vs} = -\int_A \mathbf{r}(x, y) \times \tilde{\mathbf{v}}_t(x, y) \sigma_2 p(x, y) dA \quad (30)$$

It should be noted that if  $p_n(x, y)$  in (28) is constant, then  $u$  will also be constant, allowing for easy pre-computation.

The friction forces are simulated with the same example as in Fig. 5, and the reduced planar LuGre model is compared with the distributed model, see Fig. 13. It can be observed that the reduced model does not exactly replicate the behaviour of the distributed model.

### B. Limitations with the ellipsoid approximation

The ellipsoid approximation of the limit surface is often considered a good approximation for two main reasons. First, it is computationally simple, which makes it practical for various applications. Second, the shape of the limit surface visually resembles an ellipsoid, as depicted in Fig. 14 and 16. However, the shape of the limit surface can be deceiving. Another crucial factor to consider is the correspondence between a given velocity and its location on the limit surface.

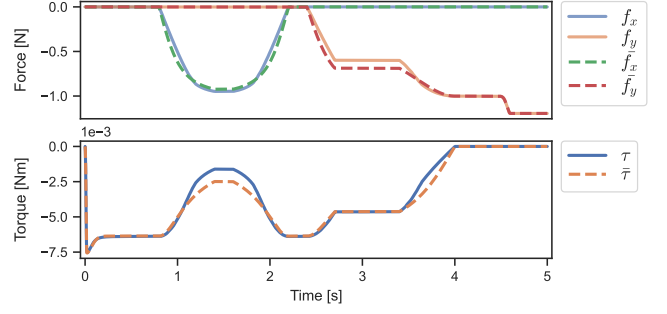


Fig. 13: The reduced model with the ellipsoid approximation compared with the distributed model for the simulation in Fig. 5. For the reduced model the forces are denoted as  $\bar{f}_x$ ,  $\bar{f}_y$  and  $\bar{f}_\tau$ .

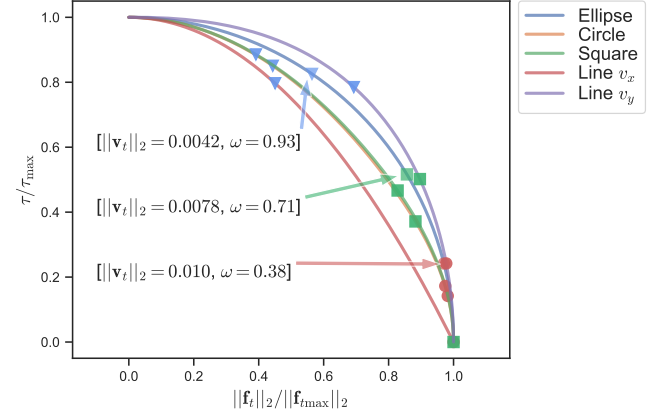


Fig. 14: The limit curves for different contact surfaces compared with the ellipse approximation of a circle contact. The markers on each curve indicate the position of a specific velocity. In the case of the line contact, the tangential velocity  $\mathbf{v}_t$  was tested along both the x-axis and y-axis, whereas for all other curves, only the x-axis was taken into consideration.  $101 \times 101$  cells were used with  $p = 0$  from table I, i.e. Coulomb friction.

Fig. 14 illustrates that the position on the limit surface associated with a particular velocity is highly correlated with the contact surface shape. Even for a circular shape, the ratio between torque and tangential force can vary significantly from the ellipsoid approximation. This is the main reason for the discrepancy observed in Fig. 13 between the reduced model and the distributed model. Based on this observation, it becomes evident that the ellipsoid approximation may be a less accurate approximation than previously suggested in the literature. While it still has many practical use cases due to its simplicity, it should be utilized with caution. In the next section, V-C, we will introduce a correction to the ellipsoid approximation method described in section V-A.

### C. Limit surface scaling

In this section, we derive a scaled bristle deflection rate that follows a pre-computed normalized limit surface. A function representing the normalized limit surface is defined as  $h(r_a, \mathbf{v}) \triangleq [f_x/f_{x\max} \ f_y/f_{y\max} \ \tau/\tau_{\max}]^T$ , the calculation of  $h(r_a, \mathbf{v})$  is further discussed in section V-D. The function  $h(r_a, \mathbf{v})$  is used to compute the corresponding unsigned steady-state bristle deflection for the limit surface as:

$$|\mathbf{z}_{ss,LS}| = \frac{\mathbf{S} |h(r_a, \mathbf{v})| g(v_n)}{\sigma_0} \quad (31)$$

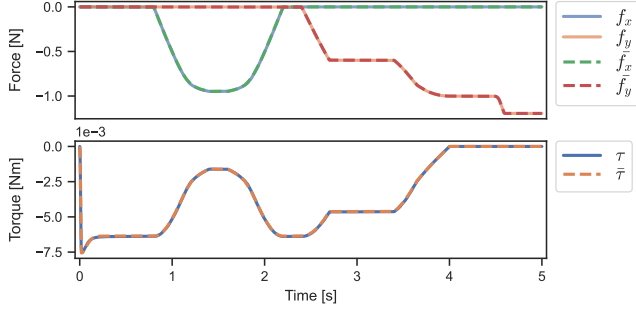


Fig. 15: Simulated forces from the reduced friction model ( $\bar{f}_x$ ,  $\bar{f}_y$  and  $\bar{\tau}$ ) with the limit surface correction, along with the forces from the distributed model. See Fig. 5 for simulation details.

where the matrix  $\mathbf{S} = \text{diag}([1 \ 1 \ r_a])$ , scales the normalized torque depending on the contact size. The sign of the steady-state bristle deflection depends on the velocity  $\mathbf{A}\mathbf{v}$ . Including the sign of the velocity in (31) results in the steady-state deflection for the reduced model:

$$\mathbf{z}_{ss} = \frac{\mathbf{w}g(v_n)}{\sigma_0} \quad (32)$$

where  $\mathbf{w} = \text{sgn}(\text{diag}(\mathbf{A}\mathbf{v}))\mathbf{S}|h(r_a, \mathbf{v})|$  and unravelling (32) gives the bristle deflection rate:

$$\dot{\mathbf{z}} = \left[ \mathbf{w} - \mathbf{z} \frac{\sigma_0}{g(v_n)} \right] v_n \quad (33)$$

where  $v_n$  is necessary for the bristle deflection rate but does not affect the steady-state deflection. The Elasto-Plastic version can be formulated as:

$$\dot{\mathbf{z}} = \left[ \mathbf{w} - \mathbf{z} \beta(\mathbf{S}^{-1}\mathbf{z}, \mathbf{S}^{-1}\mathbf{w}v_n) \frac{\sigma_0}{g(v_n)} \right] v_n \quad (34)$$

where  $\beta(\cdot, \cdot)$  is the function defined in (17), here we use three-dimensional vectors as input. It is necessary to scale the input to  $\beta(\cdot, \cdot)$  with  $\mathbf{S}^{-1}$  to ensure all elements have the same units. The forces at CoP are calculated with (27) using the bristle deflection rate from (34). The bristle deflection rate can also be bounded with the same method described in section IV-C.

Fig. 15 compares the reduced model with the limit surface correction to the planar distributed model. It demonstrates that the limit surface correction allows the model to closely match the behaviour of the distributed model. This approach requires pre-computing the normalized limit surface but allows changes in the normal force or contact surface size without the need for recalculations. The subsequent sections, V-D and V-E, explain the pre-computation and skew variables in detail.

#### D. Pre-computation of limit surface

In the preceding section V-C, we used the normalized limit surface function  $h(r_a, \mathbf{v})$ , see Fig. 16, to calculate the scaled bristle deflection. Here, we introduce a method for pre-computing  $h(r_a, \mathbf{v})$  as a hash map with bilinear interpolation. To pre-compute  $h(r_a, \mathbf{v})$ , velocity points  $\mathbf{v}$  are sampled uniformly with spherical coordinates  $0 \leq \theta \leq 2\pi$  and  $0 \leq \phi \leq \pi/2$ , see Fig. 17, where  $\theta$  represents the direction of the tangential velocity and  $\phi$  represents the ratio between sliding and spinning motion. Four neighbouring samples make

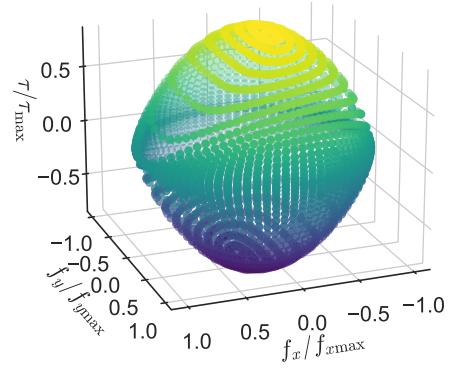


Fig. 16: Normalized limit surface with Coulomb friction for a gradient line contact.

up a cell, see Fig. 17. As we assume equal friction properties in all directions, it suffices to sample only half of the sphere. Let  $N_{LS}$  represent the number of cells between  $0$  to  $\pi/2$  [rad], and each cell on the sphere can be indexed with a unique hash map index:

$$c_i = N_{LS}\theta_i + \phi_i \quad (35)$$

where  $\theta_i$  and  $\phi_i$  are the indices along  $\theta$  and  $\phi$ , respectively. To compute the corresponding force wrench, we utilize the steady-state interpolation method described in Section IV-E with the parameters  $p = 0$  from table I, and the force wrench is normalised with the corresponding maximum force. The majority of the critical dynamics of the limit surface occur when the CoR lies within the contact area, therefore, the tangential velocities are scaled with  $r_a$  to give a more even distribution of sampled forces.

To retrieve the normalized force wrench from  $h(r_a, \mathbf{v})$ , the angle  $\theta$  can be retrieved from a given velocity vector  $\mathbf{v}$  by:

$$\theta = \begin{cases} \text{atan2}(v_y, v_x) & \omega \geq 0 \\ \text{atan2}(v_y, v_x) + \pi & \omega < 0 \end{cases} \quad (36)$$

where  $\theta$  always belongs to  $0 \leq \theta < 2\pi$ . For  $\phi$ , only the top half of the limit surface is considered:

$$\phi = \text{atan2}(r_a|\omega|, \|\mathbf{v}_t\|) \quad (37)$$

where  $r_a$  compensates for the stretched velocity sphere and allows the contact surface to be re-sized without re-calculation of  $h(r_a, \mathbf{v})$ .

The hash map index can be retrieved by calculating the corresponding indices of the angles:

$$\theta_i = \text{floor}\left(\frac{2\theta N_{LS}}{\pi}\right) \quad (38)$$

$$\phi_i = \text{floor}\left(\frac{2\phi N_{LS}}{\pi}\right) \quad (39)$$

and then the hash map key is calculated with equation (35). Within each cell, we employ bilinear interpolation, taking advantage of the residuals obtained from the flooring process:

$$\Delta\theta_i = \frac{2\theta N_{LS}}{\pi} - \text{floor}\left(\frac{2\theta N_{LS}}{\pi}\right) \quad (40)$$

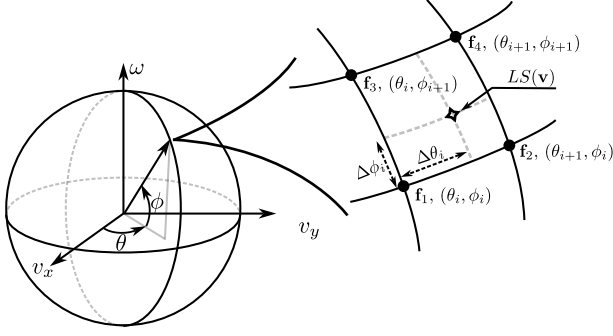


Fig. 17: Illustrates the spherical coordinates used to sample the limit surface and the bilinear interpolation of a cell on the pre-computed limit surface.

$$\Delta\phi_i = \frac{2\phi N_{LS}}{\pi} - \text{floor}\left(\frac{2\phi N_{LS}}{\pi}\right) \quad (41)$$

which range between 0 and 1, see Fig. 17. The residuals are used to interpolate between the four normalized force wrenches in a cell, yielding the output of  $h(r_a, \mathbf{v})$ .

### E. Skew variables

In this section, the estimation of the skew variables  $s_x$  and  $s_y$ , based on  $h(r_a, \mathbf{v})$  is presented. The skew variables play a crucial role in cases where the CoR coincides with the CoP, but the contact results in non-zero tangential friction forces, as depicted in Fig. 18 and 20. The skew variables add a virtual tangential velocity based on  $\omega$  to simulate the correct tangential forces. To determine the skew variables, we define a point  $\mathbf{p}_s = [\Delta x \ \Delta y]^T$  so that when CoR is aligned with  $\mathbf{p}_s$ , all tangential friction forces are cancelled out, see Fig. 18. Algorithm 1 estimates the location of  $\mathbf{p}_s$  by iteratively updating  $\mathbf{v}$  to minimize the normalized tangential forces from  $h(r_{as}, \mathbf{v})$ . Fig. 19 illustrates the velocity update in algorithm 1, the corresponding velocity to the normalized forces is estimated with an ellipsoid approximation without the skew variables.  $r_{as}$  is the  $r_a$  used during the pre-calculation. The position of  $\mathbf{p}_s$  can be pre-computed for a given contact surface and the skew variables can then be approximated by:

$$s_x = -\frac{r_a}{r_{as}} s_n \Delta y \quad \text{and} \quad s_y = \frac{r_a}{r_{as}} s_n \Delta x \quad (42)$$

where  $s_n \in [0, 1]$  is a scaling factor that depends on the ratio between  $\omega$  and the tangential velocity  $\mathbf{v}_t$ .  $s_n$  is necessary as the virtual velocity is only accurate when CoR is close to CoP.  $s_n$  is approximated by:

$$s_n = \frac{2}{\pi} \text{atan2}\left(|\omega| r_a, \sqrt{\left(\frac{v_x \Delta x}{\|\mathbf{p}_s\|}\right)^2 + \left(\frac{v_y \Delta y}{\|\mathbf{p}_s\|}\right)^2}\right) \quad (43)$$

where  $\mathbf{v}_t$  is scaled depending on each component's contribution to the virtual velocity. The scaling factor  $s_n$  decreases as the CoR moves farther away from CoP.

## VI. RESULTS

This section presents the results of the proposed friction models. First, the reduced model is compared to the planar distributed friction model using a fixed velocity profile. Then,

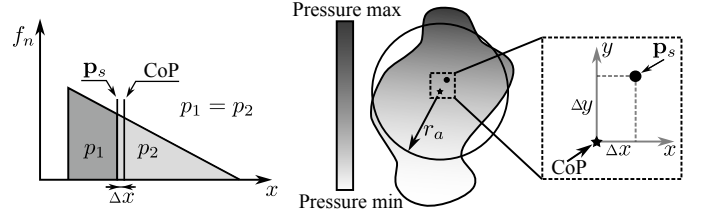


Fig. 18: The left-hand side illustrates that CoP and  $\mathbf{p}_s$  do not coincide for a gradient line contact. The  $\mathbf{p}_s$  for a 1D surface has an equal amount of pressure on either side,  $p_1 = p_2$ , and a rotation around  $\mathbf{p}_s$ , therefore, generates zero tangential force. CoP has zero moments due to the pressure, but a rotation around CoP can generate tangential forces. The right-hand side illustrates the concept for a 2D surface, where  $\mathbf{p}_s$  is a rotation point with zero tangential forces.

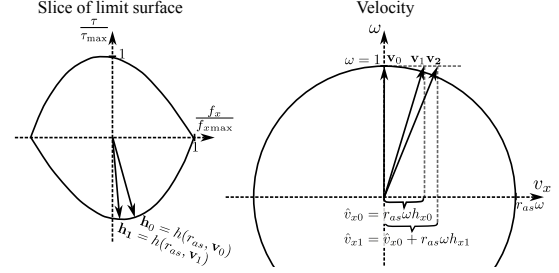


Fig. 19: Iterations in algorithm 1. The algorithm finds a velocity  $\mathbf{v}$  where the tangential forces are zeros while the surface is rotating. The left-hand side illustrates a slice of the normalised limit surface for a gradient line contact, and the right-hand side illustrates the velocity update.

in section VI-B, the computational cost is assessed and the pre-computation time is analyzed. Moreover, the planar Elasto-Plastic extension and the drifting behaviours under oscillating loads are investigated in section VI-C. Finally, the friction models are simulated using an in-hand stick-slip experiment to assess their practical applicability.

All experiments are conducted on a single core of an Intel i7-1185G7 processor. Unless explicitly stated otherwise, the experiments adopt the settings in table III. To ensure a fair comparison, the friction models are implemented in C++ and compiled as a Python module using pybind11 [34].

### Algorithm 1 Find CoR with zero tangential friction

---

```

 $\omega = 1$ 
 $[h_x \ h_y \ h_\tau]^T = h(r_{as}, \mathbf{v} = [v_x = 0 \ v_y = 0 \ \omega])$ 
 $\hat{v}_{x0} = \hat{v}_x = r_{as} \omega h_x$ 
 $\hat{v}_{y0} = \hat{v}_y = r_{as} \omega h_y$ 
while  $\sqrt{h_x^2 + h_y^2} > \text{tol}$  do
     $[h_x \ h_y \ h_\tau]^T = h(r_{as}, \mathbf{v} = [\hat{v}_x \ \hat{v}_y \ \omega])$ 
    if  $\hat{v}_{x0} \neq 0$  then
         $\hat{v}_x \leftarrow \hat{v}_x (r_{as} \omega h_x + \hat{v}_{x0}) / \hat{v}_{x0}$ 
    if  $\hat{v}_{y0} \neq 0$  then
         $\hat{v}_y \leftarrow \hat{v}_y (r_{as} \omega h_y + \hat{v}_{y0}) / \hat{v}_{y0}$ 
     $\Delta x = -\hat{v}_y / \omega$ 
     $\Delta y = \hat{v}_x / \omega$ 
return  $\mathbf{p}_s = [\Delta x \ \Delta y]^T$ 

```

---

TABLE III: Simulation settings

Parameters (table I)	$p = 1$
Step time	$dt = 1e-4$
Contact area	$0.02 \times 0.02 \text{ m}^2$
Number of cells	$21 \times 21$
Pre-computation resolution	$N_{LS} = 20$
Algorithm 1: $\text{tol}$	$1e-6$

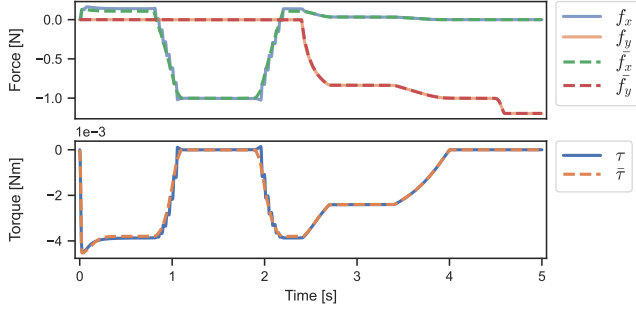


Fig. 20: Forces from a gradient line contact following the velocity profile in Fig. 5. The figure shows both the distributed model and the reduced model ( $\bar{f}_x$ ,  $\bar{f}_y$  and  $\bar{\tau}$ ).

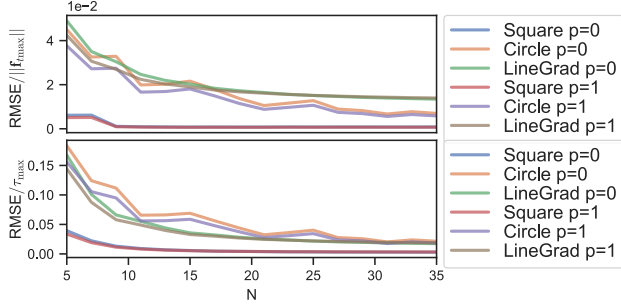


Fig. 21: The normalized RMSE for the reduced model over the number of cells ( $N \times N$ ) used during pre-computation. The top plot is for tangential friction and the bottom is for torque. The ground truth is calculated with  $101 \times 101$  cells.

#### A. Reduced vs planar distributed model

In the previous section V, the reduced model and planar distributed model were compared in the context of a circular contact surface with a fixed velocity profile, Fig. 5. The same experiment is conducted but with a gradient line contact, and the resulting friction forces are depicted in Fig. 20. It is evident that the friction forces and their transitions exhibit significant differences compared to those observed with a circular contact. Furthermore, it should be noted that in regions where pure rotation around the CoP occurs, the tangential friction force is non-zero. The reduced model addresses this by incorporating the skew variables. Lastly, it is worth observing that the reduced model does not exhibit the discrete stepping effect seen in the distributed model for linear shapes. This advantage arises due to the utilization of bilinear interpolation during the pre-computation stage.

For the planar reduced model, the normalized RMSE was calculated, see Fig. 21. This experiment is akin to the one depicted in Fig. 9, except that here the number of cells corresponds to the pre-computation. The baseline is the planar distributed model computed with  $101 \times 101$  cells. Comparing the RMSE values from Fig. 9 and 21, it can be observed that the results are comparable. The reduced model exhibits a slight advantage due to the bilinear interpolation.

#### B. Pre-computation and execution time

The primary motivation behind the reduced model is its computational efficiency, as it offers notable speed advantages irrespective of the number of cells employed, as shown in table

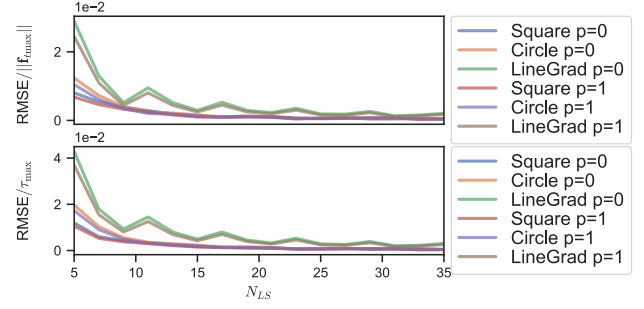


Fig. 22: The normalized RMSE for the reduced model over different resolutions  $N_{LS}$  of the pre-computed limit surface. The ground truth is calculated with  $N_{LS} = 100$ , otherwise the settings in table III are used.

IV. For instance, with  $21 \times 21$  cells, the reduced model proves to be approximately 80 times faster than the distributed model, compare table II and IV. Importantly, this improved speed does not compromise the accuracy significantly, as demonstrated by the similarity between Fig. 9 and 21.

The values presented in tables II and IV represent averages from 10 runs for each configuration. The pre-computation time demonstrates a linear relationship with the number of cells ( $N \times N$ ), as outlined in table IV. It is worth noting that if the contact shape changes, the pre-computed variables necessitate recalculation. Additionally, the second factor affecting pre-computation is  $N_{LS}$ , which characterizes the resolution of the pre-computed limit surface, see table V. The total number of sampled cells amounts to  $4N_{LS}^2$ . Fig. 22 illustrates the normalized RMSE dependency on  $N_{LS}$  for the velocity profile depicted in Fig. 5, with the baseline of  $N_{LS} = 100$ . The observed trend in Fig. 22 indicates rapid convergence to low error values for square and circular contacts, whereas the gradient line contact exhibits slower convergence. This slower convergence can be attributed to the less uniform force distribution when sampled with spherical coordinates, as illustrated in Fig. 16.

#### C. Drifting with oscillating tangential and normal load

In this section, the planar Elasto-Plastic extension is tested on both planar friction models under oscillating loads. The simulation is conducted with a 1 kg disc having a radius of 0.05 [m] on a flat surface, and the pose of the disc is tracked. In the first experiment, a tangential load equivalent to 1/12 of the force required to initiate slip is applied. After one second, an oscillation is introduced. At three seconds, an oscillating torque of approximately 1/6 of the torque required for slippage is applied, see Fig. 6. For the planar distributed model, the Elasto-Plastic extension mitigates the

TABLE IV: Computational cost (reduced model)

$N$	5	9	13	17	21	25	29	33
Pre-compute [s]	2.4e-2	5.4e-2	1.0e-1	1.8e-1	2.6e-1	3.7e-1	4.9e-1	6.3e-1
Running [it/s]	8.7e5	8.5e5	7.7e5	8.6e5	8.7e5	8.6e5	8.6e5	8.6e5

TABLE V: Computational cost  $N_{LS}$  (reduced model)

$N_{LS}$	5	9	13	17	21	25	29	33
Pre-compute [s]	2.2e-2	5.8e-2	1.1e-1	1.9e-1	2.9e-1	3.9e-1	5.3e-1	7.0e-1

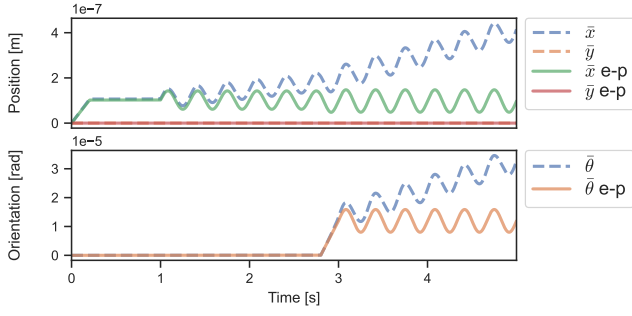


Fig. 23: The reduced planar LuGre model exhibits drift when the oscillating tangential loads from Fig. 6 are applied, and the Elasto-Plastic (e-p) extension of the reduced model mitigates the drifting. Simulated with a 1 [kg] disc with a 0.05 [m] radius.

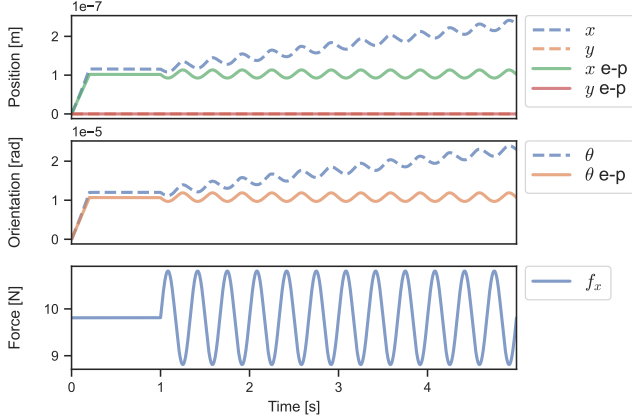


Fig. 24: The distributed planar LuGre model exhibits drift when an oscillating normal load is applied together with a constant tangential load, and the Elasto-Plastic (e-p) extension mitigates the drifting, although oscillations in displacements still persist. Simulated with a 1 [kg] disc with a 0.05 [m] radius.

drifting observed in the LuGre model. This improvement is similar to the one-dimensional case described in [10]. The same experiment is conducted for the reduced model, as shown in Fig. 23. Similarly, drifting occurs when the Elasto-Plastic extension is not utilized, but when it is employed, no drifting is observed. Here, there is a slight increase in the amplitude of the displacement oscillations when the torque is added.

Furthermore, drifting in displacement occurs when an oscillating normal load is applied with a fixed tangential load, as depicted in Fig. 24. The same disc is used, and a constant force of  $f_x = 1$  [N] and  $f_\tau = 0.03$  [Nm] is applied. The normal load oscillates with an amplitude of 1 [N]. From the results in Fig. 24, it can be observed that the Elasto-Plastic extension mitigates the drifting. However, the oscillations in displacement persist. Similar trends are observed in the results obtained from the reduced model, as shown in Fig. 25.

#### D. In-hand slip-stick

In this section, a simulation is performed on a rectangular object placed in a parallel gripper. The object has the dimensions of  $0.15 \times 0.08$  [m] and weighs 0.2 [kg]. Two cases are considered: case 1, where the Center of Mass (CoM) is positioned 25 [mm] from the Center of Area (CoA), and case 2, where the CoM is placed 2 [mm] from the CoA, as

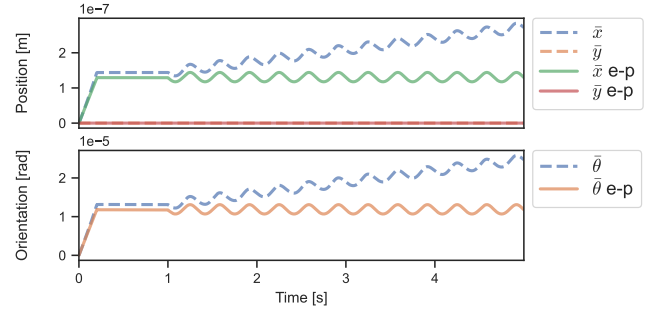
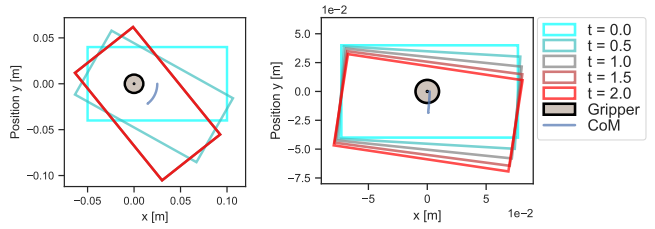


Fig. 25: The reduced planar LuGre model also exhibits drift when an oscillating normal load is applied together with a constant tangential load. Similarly to the distributed model (Fig. 24), the Elasto-Plastic (e-p) extension mitigates the drifting. Simulated with a 1 [kg] disc with a 0.05 [m] radius.



(a) Case 1: CoM 25 [mm] to CoA.

(b) Case 2: CoM 2 [mm] to CoA.

Fig. 26: Snapshots from simulation using the sinusoidal normal force, the snapshots correspond to simulations in Fig. 27 (left) and 28 (right).

illustrated in Fig. 26. For each case, two different normal force profiles are tested,  $f_{n1}$  and  $f_{n2}$ , see Fig. 27 and 28. In case 1, a larger normal force is required to initiate sticking, and the CoA behaves akin to a pivot point, as depicted in Fig. 26a. Fig. 27 demonstrates that both normal force profiles result in a similar displacement of the CoM.

In case 2, there is a more noticeable combined rotational and tangential motion, see Fig. 26b. The two normal force profiles depicted in Fig. 28 are tested for the three different contact surfaces presented in Fig. 8. The results are shown in Fig. 28, 29, and 30. In this case, the choice of the normal force profile influences the object's trajectory. With  $f_{n2}$ , a motion closer to pivoting is observed compared to  $f_{n1}$ . The circular and square contacts exhibit similar motions, while the gradient line contact results in a different trajectory. When  $f_{n1}$  is applied, the object held by the gradient line contact initially slips in both tangential and angular directions, but later only slips in the tangential direction. This occurs because the CoM quickly aligns under the CoP, resulting in no moment generated by gravity. With  $f_{n2}$ , the gradient line contact fails to generate the necessary torque for initial stiction. Two factors contribute to this behaviour. First, the gradient line contact has a CoP located farther from the initial CoM, resulting in higher torque from gravity. Second, the limit surface for the gradient line differs from that of the circular or square contact and exhibits a bias toward a lower torque ratio, as seen in Fig. 14.

Based on Fig. 27 to 30, it can be concluded that both friction models yield similar motions. Any disparities in the friction forces are integrated when calculating the object dynamics, and even a small difference can lead to significantly different motions.

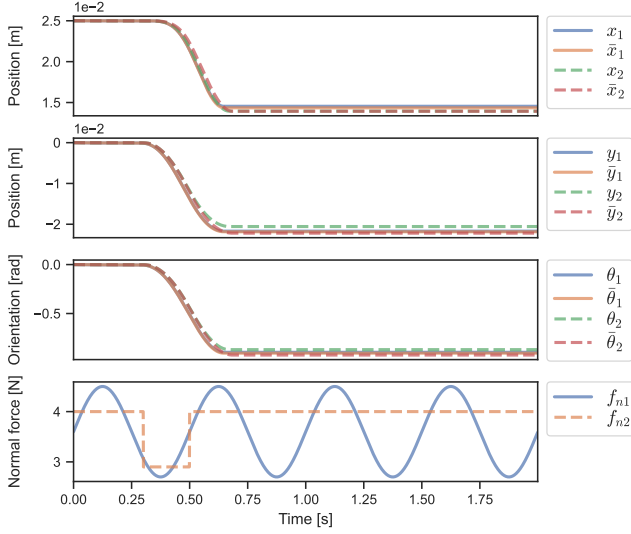


Fig. 27: Case 1: circular contact surface (0.01 [m] radius) with CoM is placed 25 mm from CoA on the x-axis. The pose of the CoM is tracked and  $\bar{\cdot}$  denotes the reduced friction model. The subscript referees to which normal force profile is used ( $f_{n1}$  or  $f_{n2}$ ).

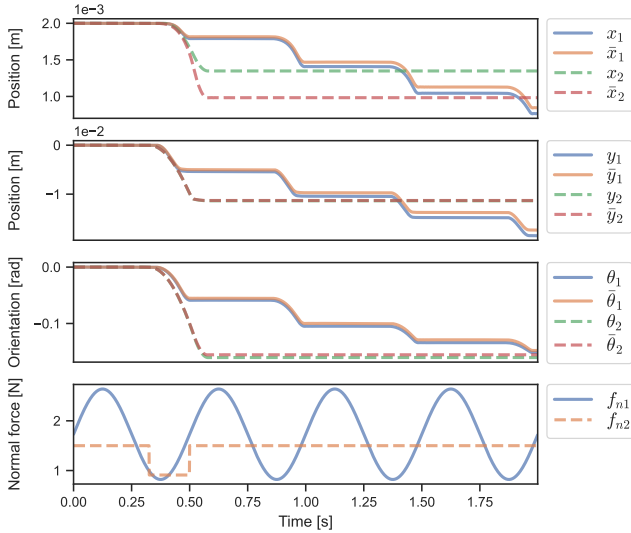


Fig. 28: Case 2: simulation with a circular contact surface (0.01 [m] radius) when CoM is placed 2 mm from CoA on the x-axis. The pose of the CoM is tracked and  $\bar{\cdot}$  denotes the reduced friction model. The subscript referees to which normal force profile is used ( $f_{n1}$  or  $f_{n2}$ ).

## VII. CONCLUSION

In this paper, we have presented a distributed planar friction model that extends the LuGre model. The Elasto-Plastic model has been adapted for the planar case, and the deflection of bristles has been bounded for numerical stability. The planar distributed model requires numerical approximations to be solved, which can be computationally intensive. To address this, we have introduced a reduced planar friction model that offers significant computational speedup while maintaining similar dynamics to the distributed model. Although the reduced model requires some pre-computation, its efficiency makes it a compelling alternative.

Nevertheless, there are still numerous challenges to tackle in friction modelling and the integration of friction models with

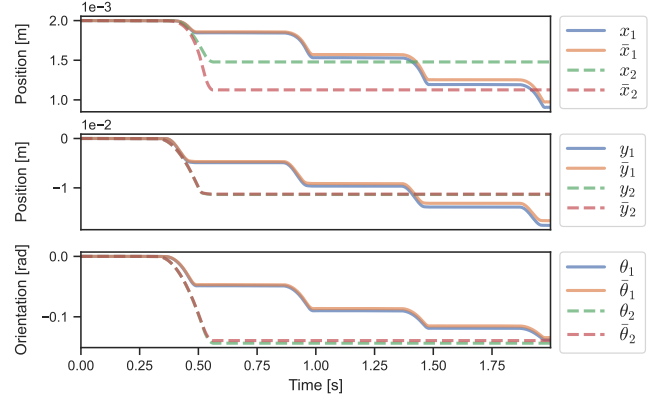


Fig. 29: Simulation from Fig. 28 but with a  $0.02 \times 0.02$  [m<sup>2</sup>] square contact surface.

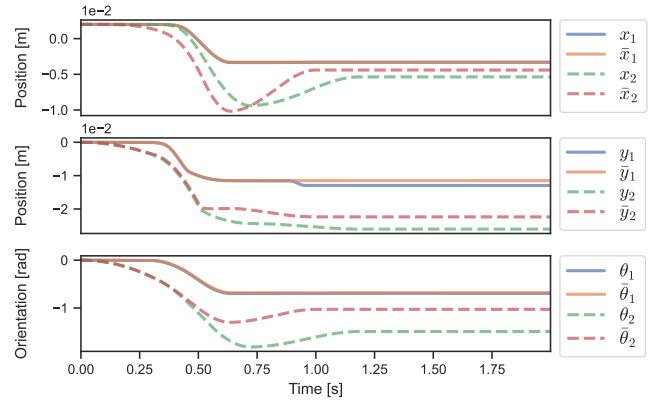


Fig. 30: Simulation from Fig. 28 but with a 0.02 [m] gradient line contact surface. The line contact is rotated so the pressure gradient is the largest in  $x < 0$  and smallest in  $x > 0$ .

solvers and object dynamics. Integrating these models with advanced solvers could help alleviate issues such as undesired oscillations caused by numerically stiff methods in conjunction with object dynamics. Additionally, in our current approach, the limit surface needs to be re-computed whenever the shape of the contact surface changes. Future research could explore the possibility of generalizing the pre-computation for all contact shapes and devising efficient methods for categorizing and identifying contact shapes. The proposed friction models hold potential for developing tactile-based perception, in-hand control of sliding objects or object manipulation based on controllable contact surfaces. However, to further advance planar friction models, it would be advantageous to establish an accessible and comprehensive benchmark based on real-world experiments.

## REFERENCES

- [1] L. Natale and G. Cannata, “Tactile sensing,” in *Humanoid Robotics: A Reference*, pp. 1–24, Springer Netherlands, 2017.
- [2] C. C. Kemp, A. Edsinger, and E. Torres-Jara, “Challenges for robot manipulation in human environments [grand challenges of robotics],” *IEEE Robotics & Automation Magazine*, vol. 14, no. 1, pp. 20–29, 2007.
- [3] E. Berger, “Friction modeling for dynamic system simulation,” *Appl. Mech. Rev.*, vol. 55, no. 6, pp. 535–577, 2002.
- [4] V. Makoviychuk, L. Wawrzyniak, Y. Guo, M. Lu, K. Storey, M. Macklin, D. Hoeller, N. Rudin, A. Allshire, A. Handa, *et al.*, “Isaac gym: High performance gpu-based physics simulation for robot learning,” *arXiv preprint arXiv:2108.10470*, 2021.

- [5] C. Lacoursière, M. Linde, Y. Lu, and J. Trinkle, "A framework for data exchange and benchmarking of frictional contact solvers in multibody dynamics," in *ECCOMAS Thematic Conference on Multibody Dynamics*, pp. 2–3, 2015.
- [6] P. R. Dahl, "A solid friction model," tech. rep., Aerospace Corp El Segundo Ca, 1968.
- [7] K. Johansson and C. Canudas-de Wit, "Revisiting the lugre friction model," *IEEE Control Systems Magazine*, vol. 28, no. 6, pp. 101–114, 2008.
- [8] R. STRIBECK, "Die wesentlichen eigenschaften der gleit-und rollen-lager [the key qualities of sliding and roller bearings]," *Z. Vereines Seutscher Ing.*, vol. 46, pp. 1432–1437, 1902.
- [9] C. C. De Wit and P. Tsiotras, "Dynamic tire friction models for vehicle traction control," in *Proceedings of the 38th IEEE conference on decision and control (Cat. no. 99CH363304)*, vol. 4, pp. 3746–3751, IEEE, 1999.
- [10] P. Dupont, B. Armstrong, and V. Hayward, "Elasto-plastic friction model: contact compliance and stiction," in *Proceedings of the 2000 American control conference. ACC (IEEE cat. no. 00CH36334)*, vol. 2, pp. 1072–1077, IEEE, 2000.
- [11] Y. Liu, J. Li, Z. Zhang, X. Hu, and W. Zhang, "Experimental comparison of five friction models on the same test-bed of the micro stick-slip motion system," *Mechanical Sciences*, vol. 6, pp. 15–28, 03 2015.
- [12] F. Marques, Ł. Woliński, M. Wojtyra, P. Flores, and H. M. Lankarani, "An investigation of a novel lugre-based friction force model," *Mechanism and Machine Theory*, vol. 166, p. 104493, 2021.
- [13] N. Do, A. Ferri, and O. Bauchau, "Efficient simulation of a dynamic system with lugre friction," *Journal of Computational and Nonlinear Dynamics - J COMPUT NONLINEAR DYN*, vol. 2, 10 2007.
- [14] Q. Wang, Q. Tian, and H. Hu, "Dynamic simulation of frictional multi-zone contacts of thin beams," *Nonlinear Dynamics*, vol. 83, pp. 1919–1937, 2016.
- [15] S. Goyal, A. Ruina, and J. Papadopoulos, "Limit surface and moment function descriptions of planar sliding," in *1989 IEEE International Conference on Robotics and Automation*, pp. 794–795, IEEE Computer Society, 1989.
- [16] S. Goyal, A. Ruina, and J. Papadopoulos, "Planar sliding with dry friction part 1. limit surface and moment function," *Wear*, vol. 143, no. 2, pp. 307–330, 1991.
- [17] R. D. Howe and M. R. Cutkosky, "Practical force-motion models for sliding manipulation," *The International Journal of Robotics Research*, vol. 15, no. 6, pp. 557–572, 1996.
- [18] M. M. Ghazaei Ardakani, J. Bimbo, and D. Prattichizzo, "Quasi-static analysis of planar sliding using friction patches," *The International Journal of Robotics Research*, vol. 39, no. 14, pp. 1775–1795, 2020.
- [19] N. Xydias and I. Kao, "Modeling of contact mechanics and friction limit surfaces for soft fingers in robotics, with experimental results," *The International Journal of Robotics Research*, vol. 18, no. 9, pp. 941–950, 1999.
- [20] A. Fakhari, M. Keshmiri, and M. Keshmiri, "Dynamic modeling and slippage analysis in object manipulation by soft fingers," in *ASME International Mechanical Engineering Congress and Exposition*, vol. 46476, p. V04AT04A056, American Society of Mechanical Engineers, 2014.
- [21] A. Bicchi, J. Kenneth Salisbury, and D. L. Brock, "Experimental evaluation of friction characteristics with an articulated robotic hand," in *Experimental Robotics II: The 2nd International Symposium, Toulouse, France, June 25–27 1991*, pp. 153–167, Springer, 1993.
- [22] J. Shi, J. Z. Woodruff, P. B. Umbanhowar, and K. M. Lynch, "Dynamic in-hand sliding manipulation," *IEEE Transactions on Robotics*, vol. 33, no. 4, pp. 778–795, 2017.
- [23] H. Hertz, "On the contact of solids—on the contact of rigid elastic solids and on hardness," *Miscellaneous papers*, pp. 146–183, 1896.
- [24] S. R. Dahmen, Z. Farkas, H. Hinrichsen, and D. E. Wolf, "Macroscopic diagnostics of microscopic friction phenomena," *Physical Review E*, vol. 71, no. 6, p. 066602, 2005.
- [25] H. Hu, A. Batou, and H. Ouyang, "Coefficient of friction random field modelling and analysis in planar sliding," *Journal of Sound and Vibration*, vol. 508, p. 116197, 2021.
- [26] E. Velenis, P. Tsiotras, and C. Canudas-de Wit, "Extension of the lugre dynamic tire friction model to 2d motion," in *Proceedings of the 10th IEEE Mediterranean conference on control and automation-MED*, pp. 9–12, 2002.
- [27] H. Kato, "Anisotropic adhesion model for translational and rotational motion," in *2014 IEEE/SICE International Symposium on System Integration*, pp. 385–391, IEEE, 2014.
- [28] H. Kato, "Friction model for planar two-dimensional motion," in *IECON 2015-41st Annual Conference of the IEEE Industrial Electronics Society*, pp. 000220–000225, IEEE, 2015.
- [29] Z. Zhou, X. Zheng, Q. Wang, Z. Chen, Y. Sun, and B. Liang, "Modeling and simulation of point contact multibody system dynamics based on the 2d lugre friction model," *Mechanism and Machine Theory*, vol. 158, p. 104244, 2021.
- [30] M. Costanzo, G. De Maria, and C. Natale, "Two-fingered in-hand object handling based on force/tactile feedback," *IEEE Transactions on Robotics*, vol. 36, no. 1, pp. 157–173, 2019.
- [31] L. Colantonio, P. Dehombreux, M. Hajžman, and O. Verlinden, "3d projection of the lugre friction model adapted to varying normal forces," *Multibody System Dynamics*, vol. 55, no. 3, pp. 267–291, 2022.
- [32] I. Rögner, "Friction modelling for robotic applications with planar motion," Master's thesis, Chalmers University of Technology, Department of Electrical Engineering, 2017.
- [33] W. H. Press, S. A. Teukolsky, W. T. Vetterling, and B. P. Flannery, *Numerical recipes 3rd edition: The art of scientific computing*. Cambridge university press, 2007.
- [34] W. Jakob, J. Rhineland, and D. Moldovan, "pybind11 – seamless operability between c++11 and python," 2017. <https://github.com/pybind/pybind11>.

## APPENDIX

### A. Proof of positive definiteness of $\mathbf{A}_{\text{sym}}$

Here it is shown that the symmetric of  $\mathbf{A}$ , namely  $\mathbf{A}_{\text{sym}} = \frac{1}{2}(\mathbf{A} + \mathbf{A}^T)$ , is a positive definite matrix by proving that its eigenvalues are positive positive. As one of the eigenvalues of  $\mathbf{A}_{\text{sym}}$  is 1 we will investigate the sign of the other two eigenvalues given by:

$$\lambda = \frac{r^2 + 1}{2} \pm \sqrt{\left(\frac{r^2 + 1}{2}\right)^2 - \left(r_a^2 - \frac{s_x^2}{4} - \frac{s_y^2}{4}\right)} \quad (44)$$

For the eigenvalues to be positive the following condition must be true:

$$4r_a^2 > s_x^2 + s_y^2 \quad (45)$$

Consider the worst case scenario of  $s_x^2 + s_y^2$  being as large as possible, that is  $s_n = 1$ , and ignore  $\frac{r_a}{r_{as}}$  as it is a linear scaling that affects both sides equally. We also consider a contact surface that consists of two points each with an infinitesimal contact area. Let point  $p_1$  be the origin with a normal force  $f_n$ , and point  $p_2$  with normal force  $\gamma f_n$  where  $0 < \gamma < \frac{1}{2}$ . Without loss of generality, we consider the two points on an one-dimensional contact line along the x-axis, that is  $s_y = 0$ . The distance between the two points is  $d$  and the location  $x$  of the CoP is then:

$$x = \frac{\gamma f_n d}{f_n(1 + \gamma)} = \frac{\gamma d}{1 + \gamma} \quad (46)$$

As the points  $p_1$  and  $p_2$  have an infinitesimal area each, the location  $p_s = s_x$  of the CoR, where no tangential forces exist, is located infinitely close to  $p_1$  as it has higher normal force. This implies  $|s_x| < |\frac{\gamma d}{1 + \gamma}|$ . The corresponding radius  $r_a$  of a circle contact when rotating around CoP can be calculated as follows:

$$r_a(f_n(1 + \gamma)) = f_n \frac{\gamma d}{1 + \gamma} + f_n(d - \frac{\gamma d}{1 + \gamma}) \quad (47)$$

and is given by:

$$r_a = \frac{d}{1 + \gamma} \quad (48)$$

If we assume the worst "one-dimensional" case as  $s_x = -\frac{\gamma d}{1 + \gamma}$  and  $s_y = 0$ , then (45) becomes  $2r_a > |s_x|$  that, in turn, yields:

$$2 \frac{d}{1 + \gamma} < \frac{\gamma d}{1 + \gamma} \quad (49)$$

which holds as  $0 < \gamma < \frac{1}{2}$ . Therefore, all eigenvalues are positive and  $\mathbf{A}_{\text{sym}}$  is positive definite for all surfaces.